EPJ manuscript No.
(will be inserted by the editor)

arXiv:nucl-th/9811019v4 10 Sep 1999

ωN final state interactions and ω-meson production from heavy-ion collisions

G.I. Lykasov[1], W. Cassing[2], A. Sibirtsev[2], M.V. Rzjanin[1]

[1][1] Joint Institute for Nuclear Research
[1]141980 Dubna, Moscow Region, Russia
[1][2] Institut für Theoretische Physik
[1]Heinrich-Buff-Ring 16, D-35392 Giessen, Germany

Received: date / Revised version: date

Abstract. We calculate the elastic and inelastic $\omega N{\to}\omega N$, ${\to}\pi N$, ${\to}\rho N$, ${\to}\rho\pi N$, ${\to}\pi\pi N$, ${\to}\sigma N$ reactions within a boson exchange approximation where the $\omega\rho\pi$ coupling constant and form factor are fixed by the reaction $\pi N{\to}\omega N$ in comparison to the experimental data. We find rather large ωN cross sections at low relative momenta of the ω-meson which leads to a substantial broadening of the ω-meson width in nuclear matter. The implications of the ωN final state interactions are studied for ω production in ${}^{12}C{+}{}^{12}C$, ${}^{40}Ca{+}{}^{40}Ca$ and ${}^{58}Ni{+}{}^{58}Ni$ reactions at about 2·A GeV within the HSD transport approach; the drastic changes of the transverse mass spectra relative to a general m_T-scaling (for π^0 and η mesons) might be controlled experimentally by the TAPS Collaboration.

PACS. 25.75.-q – 25.80.-e

1 Introduction

The properties of hadrons in a dense and hot nuclear medium are of fundamental interest with respect to the question of chiral symmetry restoration in such an environment, where a new phase of strongly interacting matter might be encountered [1,2,3,4]. The properties of vector mesons here are of particular interest since these can be studied experimentally via their decay to dileptons. Whereas the ρ-meson spectral function in the medium has been discussed to a large extent [5,6,7,8] the properties of the ω-meson in dense matter especially at finite relative momentum are achieving increasing interest [9,10,11,12,13,14,15,16]. As in case of the ρ-meson the ω-meson properties at low baryon density are dominantly determined by the interactions with nucleons; real and imaginary parts of the scattering amplitude then are determined by dispersion relations. It is thus of fundamental interest to obtain some information about the ωN scattering cross sections which except for the channel $\pi N{\to}\omega N$ are not accessable by experiment.

In this work we address the latter question in a boson - exchange approach and study the implications from the ωN final state interactions for ω production in nucleus-nucleus reactions around 2 A·GeV in the context of present experiments by the TAPS Collaboration. In Section 2 we will calculate the various elementary ωN channels within a boson-exchange model and discuss the uncertainties due to coupling constants and form factors. The transport calculations within the HSD approach [17] for ω-meson production in nucleus-nucleus reactions will be presented in Section 3. A summary and discussion of open questions concludes this work in Section 4.

2 ωN cross sections

We start by recalling some general features of the ωN cross section. Since the ω-meson mass is about 5.5 times larger than the pion mass, at low ω-meson momenta the exothermic reactions like $\omega N{\to}\pi N$, $\omega N{\to}2\pi N$, $\omega N{\to}3\pi N$ and other channels with a production up to 5 π-mesons should be dominant and the corresponding inelastic cross section behave as $\sigma_{inel}{\simeq}1/p_\omega$, where p_ω denotes the laboratory momentum. When the total mass of the final particle becomes equal to the total mass of the incident ones, e.g. in the $\omega N{\to}\rho N$ or $\omega N{\to}\omega N$ reaction, the relevant cross section should approach some constant at low p_ω. On the other hand the endothermic inelastic reactions, where the total mass of the produced particles is larger than the initial mass, have a threshold behaviour and are more important at high energies.

The amount of the available ωN reaction channels, especially in the inelastic sector, is quite large. Thus one needs a reliable model for the ω-nucleon interaction at energies up to few GeV. The complexibility of the problem has been addressed in the recent studies from Klingl, Kaiser and Weise [12,13] and Friman [15,16], where some of the ωN reaction channels were calculated. However, as pointed out in Refs. [15,16] the calculated results are very sensitive to the parameters of the model, i.e. coupling constants, form factors, etc.

As a first step for a simplification we adopt the $\omega\rho\pi$ dominance model proposed by Gell-Mann, Sharp and Wagner [18] as well as the σ exchange approximation, which accounts for an effective two-pion exchange in the spin-isospin zero channel. In practice we restrict to the diagrams shown in Fig 1 which contain the $\omega\rho\pi$-vertex and the $\omega\sigma\omega$-vertex. In this way we

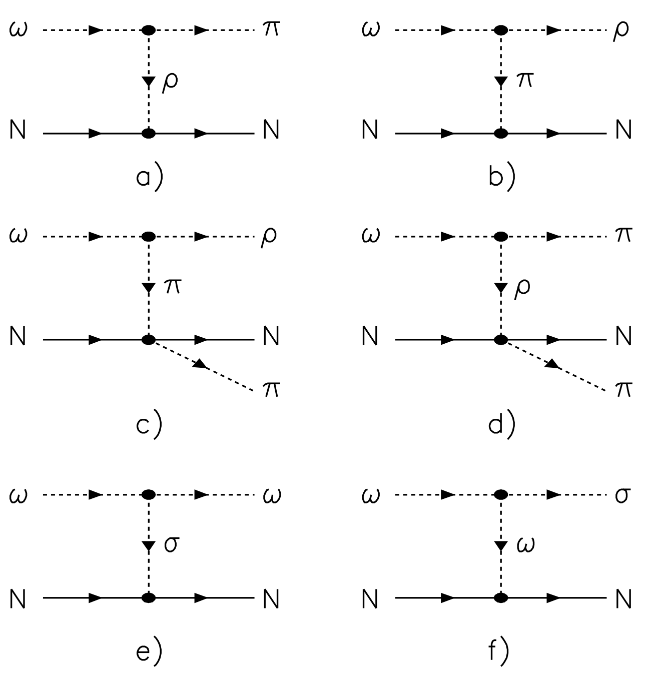

Fig. 1. The diagrams for the ωN reaction channels evaluated in the text.

expect to obtain lower bounds especially on the total inelastic scattering cross section.

One way to construct the $\omega\rho\pi$ Lagrangian is due to the current-field identities of Kroll, Lee and Zumino [19], where the isoscalar and isovector parts of the electromagnetic current – with the ω- and ρ-meson currents, respectively – can be identified. Starting with the Lagrangian for the vector-meson photoproduction on the nucleon one can construct the corresponding Lagrangian for the vector meson-nucleon interaction as in Ref. [20]. The photoproduction of ρ and ω-mesons on the nucleon close to threshold ($E_\gamma \leq 2$ GeV) has been analyzed by Friman and Soyeur [20] also within the framework of the one-boson exchange (OBE) model. In this sense the OBE model can be applied to elastic and inelastic ωN interactions. Furthermore, the relevant coupling constant $g_{\omega\rho\pi}$ as well as the corresponding form factor can be taken from the earlier analysis in Ref. [20]. In the present work we additionally consider $\omega\sigma\omega$-vertices and discuss the uncertainties related to the coupling constants and form factors at the vertices. The latter uncertainties are reduced to a large extent by the analysis of experimental data on the $\pi N \to \omega N$ (or inverse $\omega N \to \pi N$) reaction.

2.1 The channel $\omega N \to \pi N$

The $\omega N \to \pi N$ cross section can be controlled by the experimental data on the inverse reaction via detailed balance. The OBE diagram within our approach for the $\pi N \to \omega N$ reaction is described by the ρ-meson exchange as shown in Fig. 1a). For our present study we adopt an effective Lagrangian for the $\omega\rho\pi$ interaction as

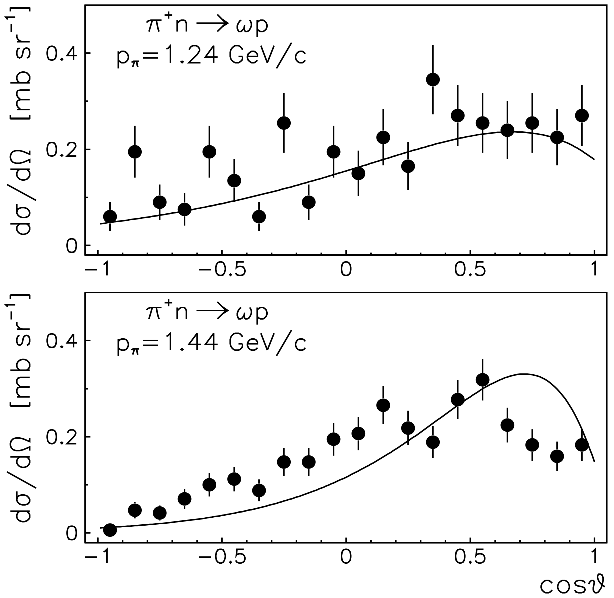

Fig. 2. Differential cross sections for the $\pi^+ n \to \omega p$ reaction at pion momenta of 1.24 GeV/c and 1.44 GeV/c. The data were taken from Ref. [27] and are shown for 100 MeV-wide c.m. energy intervals while the solid lines show our calculations.

$$\mathcal{L}_{\omega\rho\pi} = \frac{g_{\omega\rho\pi}}{m_\omega} \epsilon_{\alpha\beta\gamma\delta} \partial^\alpha \rho^\beta \partial^\gamma \omega^\delta \pi, \tag{1}$$

where the coupling constant $g_{\omega\rho\pi} = 11.79$ was evaluated from the $\omega \to 3\pi$ partial width assuming the virtual ρ model for the ω-meson decay [18]. Our result is close to $g_{\omega\rho\pi} = 10.88$ from Ref. [21]. In (1) $\epsilon_{\alpha\beta\gamma\delta}$ denotes the antisymmetric tensor while ρ, ω and π are the corresponding meson fields. The ρNN Lagrangian is taken as

$$\mathcal{L}_{\rho NN} = -g_{\rho NN} \Big(\bar{N}\gamma^\mu \tau N \cdot \rho_\mu + \frac{\kappa}{2m_N} \bar{N}\sigma^{\mu\nu}\tau N \cdot \partial_\mu \rho_\nu \Big), \tag{2}$$

where N stands for the nucleon field, τ for the Pauli matrices, $g_{\rho NN}$=3.24 according to Ref. [22], while the tensor coupling constant is given by the ratio κ=$f_{\rho NN}/g_{\rho NN}$=6.1 .

The differential cross section for the $\pi N \to \omega N$ process is given as [23]:

$$\frac{d\sigma}{dt} = \frac{g^2_{\omega\rho\pi}}{m^2_\omega} \frac{1}{8\pi\lambda(s,m^2_N,m^2_\pi)} \frac{F^2_{\omega\rho\pi}F^2_{\rho NN}}{(t-m^2_\rho)^2} \times \Bigg[-\left(g_{\rho NN}+f_{\rho NN}\right)^2 m^2_\omega q^2_\omega t + \left(g^2_{\rho NN} - \frac{f^2_{\rho NN} t}{4m^2_N} \right) \times \left\{ \frac{sin^2\theta}{8\,s}\, \lambda(s,m^2_N,m^2_\pi)\, \lambda(s,m^2_N,m^2_\omega) \right\} \Bigg] \tag{3}$$

where

$$q_\omega^2 = \frac{\lambda(t, m_\omega^2, m_\pi^2)}{4m_\omega^2}. \tag{4}$$

In Eq. (3) s is the squared invariant collision energy, t is the 4-momentum transfered from the initial to the final nucleon, θ is the production angle and

$$\lambda(x,y,z) = (x-y-z)^2 - 4yz. \tag{5}$$

For the $\omega\rho\pi$ vertex we use the form factor

$$F(t) = \frac{\Lambda^2 - m_\rho^2}{\Lambda^2 - t}. \tag{6}$$

We note that using a formfactor similar to (6) for the ρNN-vertex the energy dependence of the $\pi N \to \omega N$ production cross section as well as the differential cross sections cannot be described properly. Similar difficulties in comparing the ρ- exchange model with experimental data were found by other authors [24,25,26,27,28]. We, therefore, introduce a more general formfactor at the ρNN-vertex as[1]

$$F(t,s) = \exp\left(\beta\, t\right)\, \exp\left(-\alpha\, s\right). \tag{7}$$

To fix the cut-off Λ in the $\omega\rho\pi$ vertex as well as the parameters β and α in the ρNN vertex we fit the available experimental data on differential and total cross sections for the $\pi N \to \omega N$ reaction.

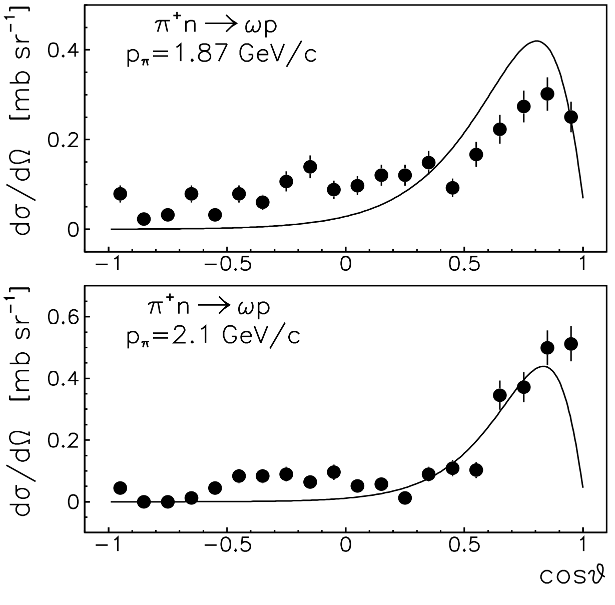

Fig. 3. Differential cross sections for the $\pi^+ n \to \omega p$ reaction at pion momenta of 1.87 GeV/c and 2.1 GeV/c. The data were taken from Ref. [27] and are shown for 100 MeV-wide c.m. energy intervals while the solid lines show our calculations.

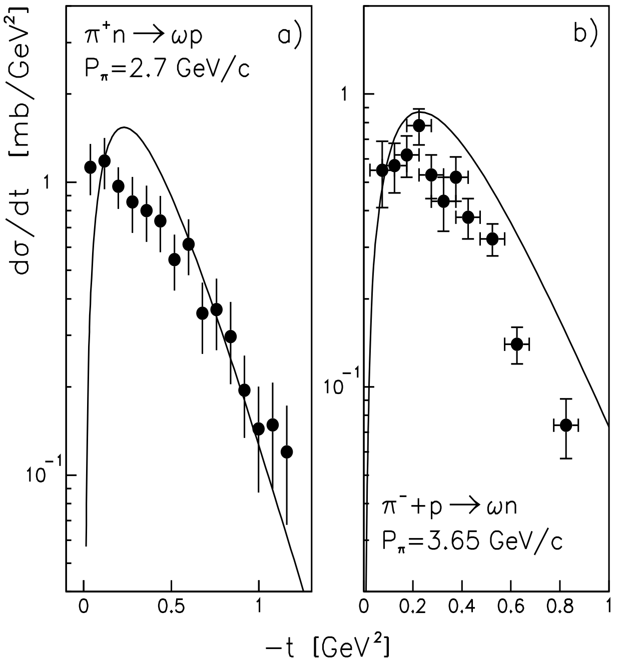

Fig. 4. The $\pi^+ n \to \omega p$ (a) and $\pi^- p \to \omega n$ (b) differential cross sections as a function of the transverse 4-momentum squared. The data were taken from Refs. [24,30] while the lines show our calculations.

Figs. 2,3 show the $\pi^+ n \to \omega p$ differential cross section [27] for pion momenta from p_π=1.24 to 2.1 GeV/c together with our calculations (solid lines). The data are shown for 100 MeV-wide $\sqrt{s}$ energy intervals centered at the pion momenta indicated in Figs. 2,3. Note, that only statistical errors are shown.

Fig. 4a) shows the $\pi^+ n \to \omega p$ differential cross section [24] at the pion momentum p_π=2.7 GeV/c together with our calculations while Fig. 4b) shows the comparison to the $\pi^- p \to \omega n$ data [30] at p_π=3.65 GeV/c.

From the fit of the experimental data with respect to the s-dependence of the cross section and the differential cross sections $d\sigma/dt$ the parameters were fixed in the following way:

$$\Lambda = 2.7\, GeV; \quad \beta = 2.3\, GeV^{-2}; \quad \alpha = 0.16\, GeV^{-2}. \tag{8}$$

Fig. 5 shows the total $\pi^+ n \to \omega p$ and $\pi^- p \to \omega n$ cross section as a function of the pion momentum. Again the data are reasonably reproduced with Λ=2.7 GeV, which we now fix for the following analysis.

The calculated cross section for the inverse reaction $\omega N \to \pi N$ is shown in Fig. 6 for Λ_1=2.7 GeV as a function of the ω-momentum in the laboratory in comparison to the experimental data obtained by detailed balance.

2.2 The channel $\omega N \to \rho N$

The $\omega N \to \rho N$ cross section can be calculated in the one-pion exchange model using the diagram in Fig. 1b). The Lagrangian for the $\omega\rho\pi$ interaction is given by Eq. (1), while the πNN Lagrangian is taken as

$$\mathcal{L}_{\pi NN} = -ig_{\pi NN} \bar{N} \gamma_5 \tau N \cdot \pi \tag{9}$$

---

[1] For a discussion of the ansatz (7) see Ref. [29] and references therein.

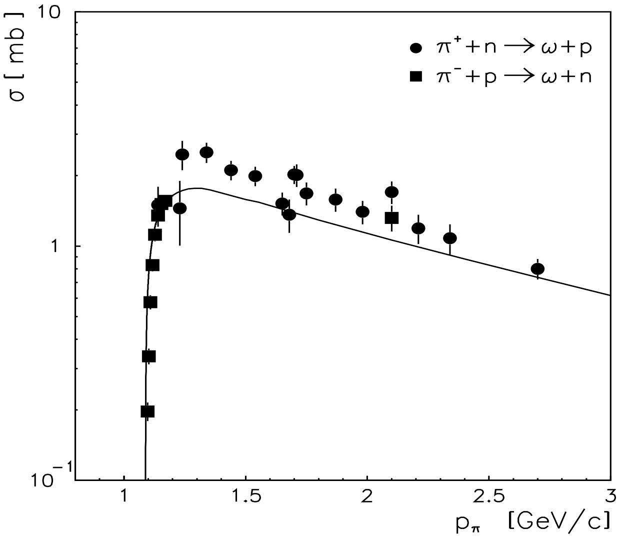

Fig. 5. The $\pi^+n\to\omega p$ (circles) and $\pi^-p\to\omega n$ (squares) total cross sections as a function of the pion momentum. The data are from Ref. [31] while the solid line shows our calculations for the cut-off parameter Λ=2.7 GeV.

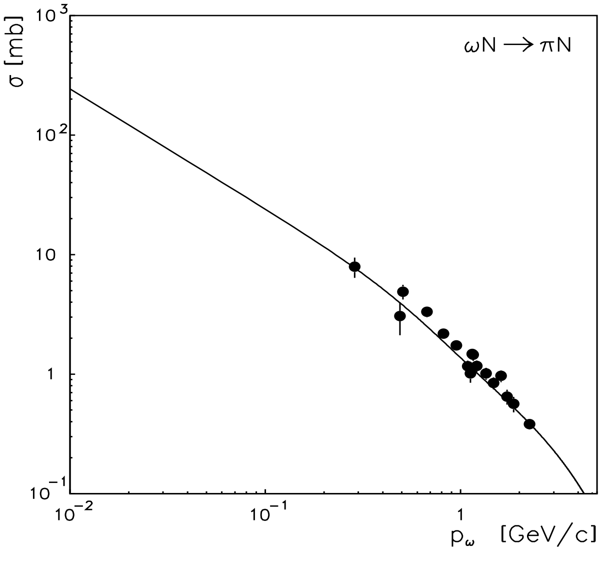

Fig. 6. The cross section for the $\omega N\to\pi N$ reaction as a function of the laboratory ω-momentum. The solid line is our calculation while the full circles show the $\omega p\to\pi^+n$ experimental data obtained by detailed balance.

with the coupling constant $g_{\pi NN}$ =13.59 [32].

The $\omega N\to\rho N$ differential cross section then is given by

$$\frac{d\sigma}{dt} = -g^2_{\pi NN}\, t\, \frac{g^2_{\omega\rho\pi}}{m^2_\omega}\, \frac{(t-m^2_\omega-m^2_\rho)^2-4m^2_\omega m^2_\rho}{96\,\pi\,\lambda(s,m^2_\omega,m^2_N)} \times \frac{F^2_{\omega\rho\pi}(t)\,F^2_{\pi NN}(t)}{(t-m^2_\pi)^2}, \qquad (10)$$

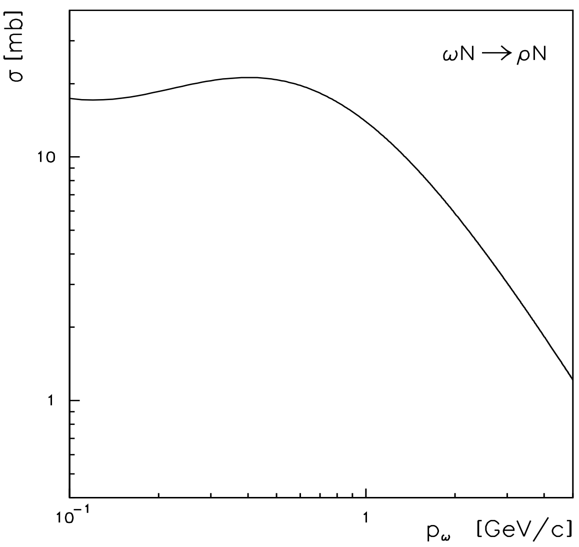

Fig. 7. The cross section for the $\omega N\to\rho N$ reaction.

where the coupling constant and the form factor for the $\omega\rho\pi$-vertex is fixed by the $\pi N\to\omega N$ calculations. The πNN form factor was taken as in Eq. (6) with the cut-off parameter $\Lambda = 1.05$ GeV in line with Ref. [33].

The resulting $\omega N\to\rho N$ cross section is shown by the solid line in Fig. 7 as a function of the ω-meson laboratory momentum; the cross section is practically constant at low momentum ($\approx$ 18 mb) and levels off at higher momenta due to the form factors involved. However, above momenta of about 200 MeV/c it is already larger than for the πN final channel.

2.3 The channel $\omega N\to\rho\pi N$

The relevant diagram for the reaction $\omega N\to\rho\pi N$ is shown in Fig. 1c) and the corresponding total cross section can be calculated by using the Berestetsky-Pomeranchuk approach [34] as

$$\sigma = \frac{1}{48\pi^2\lambda(s,m^2_N,m^2_\omega)} \int\limits_{(m_N+m_\pi)^2}^{(\sqrt{s}-m_\rho)^2} ds_1 \lambda^{1/2}(s_1,m^2_\pi,m^2_N) \times\sigma_{\pi N}(s_1)\int\limits_{t_-}^{t^+} dt\, \frac{g^2_{\omega\rho\pi}\,F^2_{\omega\rho\pi}}{m^2_\omega\,(t-m^2_\pi)^2} \times\left[\left(t-m^2_\omega-m^2_\rho\right)^2-4m^2_\omega m^2_\rho\right] \qquad (11)$$

In Eq.(11) s_1 is the squared invariant mass of the final πN system, $\sigma_{\pi N}$ is the $\pi N\to\pi N$ elastic cross section taken from Ref. [31] and

$$t^\pm = m^2_\omega + m^2_\rho - \frac{1}{2s}\left[(s+m^2_\omega-m^2_N) \times(s+m^2_\rho-s_1) \mp\lambda^{1/2}(s,m^2_\omega,m^2_N)\,\lambda^{1/2}(s,m^2_\rho,s_1)\right].\qquad (12)$$

The resulting $\omega N \to \rho\pi N$ cross section is shown in Fig. 8a) by the dashed line while the arrow indicates the corresponding reaction threshold. Now replacing the elastic $\pi N \to \pi N$ cross section in Eq. (11) by the total cross section $\pi N \to NX$ we obtain an estimate for the inclusive $\omega N \to \rho NX$ cross section, which is shown in terms of the solid line in Fig. 8a). This channel provides an inelastic ωN cross section of about $\simeq$25 mb at higher momenta.

In Fig. 8a) we have adopted the on-shell approximation [34]. The off-shell correction to the πN amplitude can be estimated e.g. as proposed by Ferrari and Selleri [35], i.e. replacing $t \to m_\pi^2$ in the λ-function of Eq. (11) and introducing the form factor

$$F(t) = \frac{\Lambda^2 - m_\pi^2}{\Lambda^2 - t} \tag{13}$$

at the $\pi N \to \pi N$ vertex.

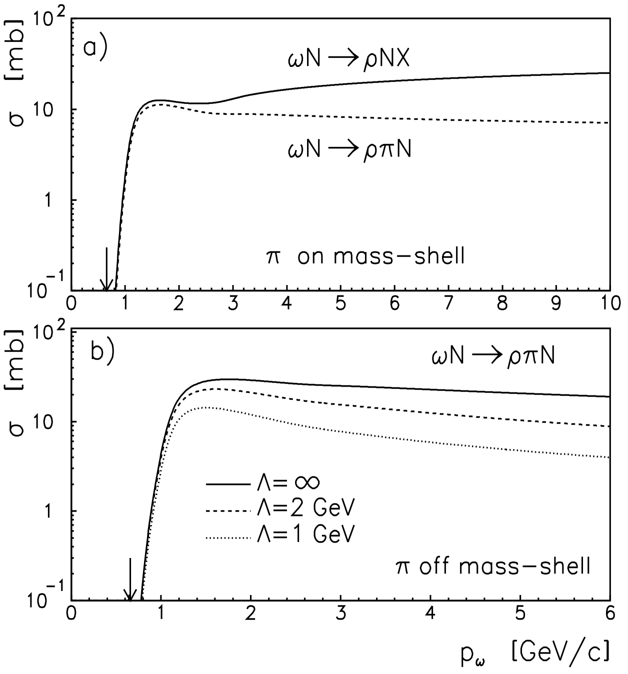

Fig. 8. a): The exclusive $\omega N \to \rho\pi N$ (dashed line) and inclusive $\omega N \to \rho NX$ cross sections calculated with the one-pion exchange model and within the on mass-shell approximation. The arrow indicates the threshold for the exclusive reaction. b): The exclusive $\omega N \to \rho\pi N$ cross section calculated within the off mass-shell approach for different cut-off parameters Λ in the $\pi N \to \pi N$ vertex.

The solid line in Fig. 8b) indicates the corresponding calculation when neglecting the form factor at the $\pi N \to \pi N$ vertex ($\Lambda = \infty$), the dashed line shows the calculation with the cut-off parameter Λ=2 GeV while the dotted line corresponds to Λ=1 GeV. Note, that the uncertainty due to the cut-off parameter is quite large when varying Λ from 1 GeV to ∞. However, the comparison between the dashed line in Fig. 8a) and the dotted line in Fig. 8b) indicates that the results obtained for Λ=1 GeV (in line with Ref. [36]) are in reasonable agreement with the on mass-shell calculations. Thus in the following we will adopt the on mass-shell approximation.

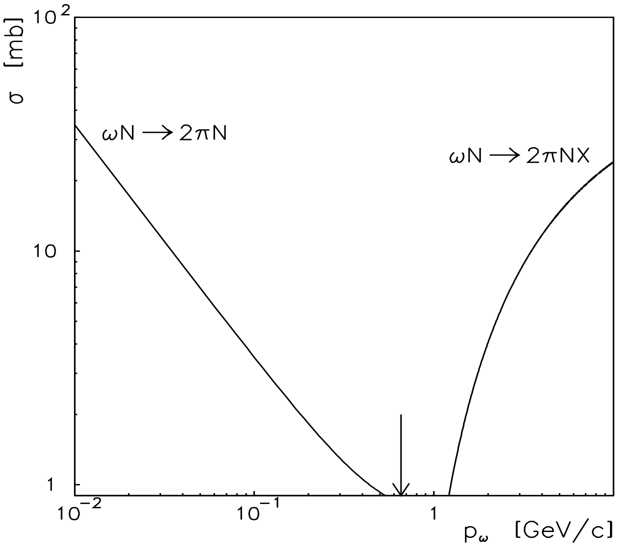

Fig. 9. The exclusive $\omega N \to 2\pi N$ and inclusive $\omega N \to \pi NX$ cross sections. The arrow indicates the $\omega N \to \pi\rho N$ threshold using the ρ pole mass. The inclusive cross section is calculated for the invariant mass of the πN-system above $m_\rho + m_N$.

2.4 The channel $\omega N \to 2\pi N$

The $\omega N \to 2\pi N$ cross section can be calculated in the ρ-meson exchange model as shown by the diagram in Fig. 1d). By taking into account the on-shell $\rho N \to \pi N$ amplitude the total cross section is given as

$$\sigma = \frac{1}{32\pi^2\,\lambda(s,m_N^2,m_\omega^2)} \int\limits_{(m_N+m_\pi)^2}^{(\sqrt{s}-m_\pi)^2} ds_1 \lambda^{1/2}(s_1,m_\rho^2,m_N^2)$$
$$\times \sigma_{\rho N\to\pi N}(s_1) \int\limits_{t_-}^{t^+} dt\, \frac{g_{\omega\rho\pi}^2\, F_{\omega\rho\pi}^2}{m_\omega^2\,(t-m_\rho^2)^2}$$
$$\times \left[\left(t+m_\omega^2-m_\pi^2\right)^2 - 4tm_\omega^2\right], \tag{14}$$

where

$$t^\pm = m_\omega^2 + m_\pi^2 - \frac{1}{2s}\left[(s+m_\omega^2-m_N^2)\right.$$
$$\left.\times(s+m_\pi^2-s_1) \mp \lambda^{1/2}(s,m_\omega^2,m_N^2)\,\lambda^{1/2}(s,m_\pi^2,s_1)\right]. \tag{15}$$

In Eq. (14) the $\rho N \to \pi N$ cross section was taken as in Ref. [37],

$$\sigma_{\rho N\to\pi N}(s_1) = \frac{\pi^2}{3}\, \frac{a}{\lambda^{1/2}(s_1,m_\rho^2,m_N^2)}$$
$$\times \frac{\Gamma^2}{(\sqrt{s_1}-M)^2 + \Gamma^2/4}, \tag{16}$$

with the parameters a=413 μb/GeV^2, M=1.809 GeV and Γ = 0.99 GeV. Note, that the function $\lambda^{1/2}$ in Eq. (14) is cancelled by Eq. (16). The cross section $\omega N \to 2\pi N$ calculated with Eq. (14) is shown in Fig. 9 and approaches 30 mb for omega momenta of 10 MeV/c, but dropps off fast with higher momentum.

Now we replace the $\rho N \to \pi N$ cross section in Eq. (14) by the total ρN cross section taken from Ref. [38] in order to estimate the inclusive $\omega N \to \pi N X$ reaction due to ρ-meson exchange. However, we replace the lower limit of the first integral in Eq. (14) by $(m_N + m_\rho)^2$, which allows us to estimate only part of the total cross section. This calculated cross section is shown in Fig. 9 together with the threshold given by the bare ρ-mass (arrow) for momenta above 1 GeV/c.

2.5 Elastic $\omega N \to \omega N$ scattering

We describe elastic ωN scattering by the sigma-exchange model shown in terms of the diagram Fig. 1e), which effectively accounts for a correlated two-pion exchange in the spin-isospin zero channel. The Lagrangian used reads

$$\mathcal{L}_{\sigma NN} = g_{\sigma NN} \bar{N} N \cdot \sigma, \tag{17}$$

$$\mathcal{L}_{\omega\sigma\omega} = g_{\omega\sigma\omega} \left(\partial^\alpha \omega^\beta \partial_\alpha \omega_\beta - \partial^\alpha \omega^\beta \partial_\beta \omega_\alpha \right) \sigma, \tag{18}$$

with the scalar coupling constant $g_{\sigma NN}$=10.54 and monopole form factors with cut-off parameter Λ=2 GeV at the σNN vertex [39].

An upper limit for the $\omega\sigma\omega$ coupling can be obtained from the $\omega \to 2\pi^0\gamma$ partial width assuming that this decay entirely proceeds through the $\omega \to \sigma\omega$ process followed by the $\omega \to \gamma$ transition due to the vector dominance model and the $\sigma \to 2\pi^0$ decay. Starting from the Lagrangian (18) and integrating over the σ spectral function Post [40] obtained $g_{\omega\sigma\omega} \approx 5.7$ taking into account the most recent data [41] on the $\omega \to 2\pi^0\gamma$ decay. A coupling $g_{\omega\sigma\omega}$=0.5 was estimated in Refs. [42,43] from the $\omega \to 2\pi^0\gamma$ decay [44] using, however, a different Lagrangian for the $\omega\sigma\omega$ interaction and replacing the σ-meson spectral function by a δ-distribution.

On the other hand, as proposed by Singer [45], the $\omega \to 2\pi\gamma$ decay may proceed also through the two-step process $\omega \to \rho\pi$ followed by the $\rho \to \pi\gamma$ transition; the data on the partial $\omega \to 2\pi^0\gamma$ width indeed can be entirely described by the latter process. A more sophisticated analysis has been performed by Fajfer and Oakes [46], who consider a three-step process $\omega \to \rho\pi$ followed by $\rho \to \pi\omega$ and as a last step the $\omega \to \gamma$ transition. They predict [46] a branching ratio for the $\omega \to 2\pi^0\gamma$ decay of 8.21×10^{-5}, which is compatible to $(7.2 \pm 2.5) \times 10^{-5}$ as quoted recently by the PDG [41].

We point out that there are no reliable constraints for the $\omega\sigma\omega$ coupling constant and in the following calculations adopt $g_{\omega\sigma\omega}$=1.76 keeping it essentially as a free parameter of the model. To demonstrate the uncertainty, we will also present final results for $g_{\omega\sigma\omega}$ = 0. Furthermore, we use a monopole form factor with cut-off parameter Λ=2.0 GeV for the $\omega\sigma\omega$ vertex. With the latter value $g_{\omega\sigma\omega}$=1.76 the resulting elastic and inelastic contributions to the ωN cross section will be quite moderate.

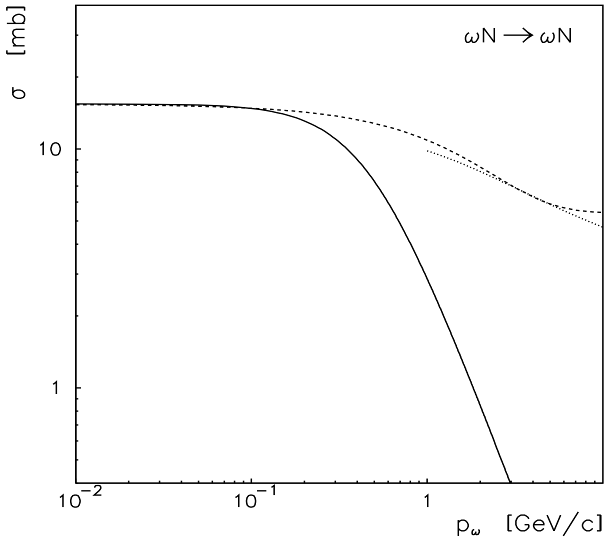

Fig. 10. The $\omega N \to \omega N$ elastic cross section. The solid line indicates the calculation within the σ-exchange model for $g_{\omega\sigma\omega}$=1.76; the dotted line is the high energy limit (20), while the dashed line shows our interpolation (21).

The elastic $\omega N \to \omega N$ cross section then can be calculated as

$$\frac{d\sigma}{dt} = \frac{g_{\sigma NN}^2 \, g_{\omega\sigma\omega}^2}{16\pi \, m_\omega^2 \, \lambda(s, m_\omega^2, m_N^2)} \, \left(4m_N^2 - t\right) \frac{F_{\omega\sigma\omega}^2 \, F_{\sigma NN}^2}{(t - m_\sigma^2)^2} \, \left(m_\omega^4 - \frac{m_\omega^2 \, t}{3} + \frac{t^2}{12} \right) \tag{19}$$

with m_σ=550 MeV. The result of this model is shown by the solid line in Fig. 10 and indicates a maximum of ≈15 mb at low relative momentum but levels off very fast for high momenta.

The high energy limit for the $\omega N \to \omega N$ elastic cross section can be taken in the Quark Model [47,48] as

$$\sigma_{\omega N \to \omega N}(s) = \frac{1}{2} \left[\sigma_{\pi^+ N \to \pi^+ N}(s) + \sigma_{\pi^- N \to \pi^- N}(s) \right], \tag{20}$$

which is shown in Fig. 10 by the dotted line above momenta of 1 GeV/c. We add that in Eq. (20) the elastic $\pi^\pm N$ cross section is taken from Ref. [49] and the identity (20) is used at the same invariant energy for the ωN- and πN-interaction.

For our following applications to heavy-ion transport simulations we interpolate the ωN elastic cross section within the range from 10 MeV/c up to 10 GeV/c as

$$\sigma_{el} = 5.4 + 10 \exp(-0.6 p_\omega) \ [\mathrm{mb}], \tag{21}$$

where p_ω denotes the laboratory momentum of the ω-meson in GeV/c. The parameterization (21) is shown additionally by the dashed line in Fig. 10.

2.6 The channel $\omega N \to \sigma N$

When incorporating the $\omega\sigma\omega$-vertex for elastic ωN scattering one has to consider this vertex also in the $\omega N \to \sigma N$ reaction due to ω-meson exchange as shown in Fig. 1f). The differential cross section for this process is given by

$$\frac{d\sigma}{dt} = \frac{g_{\omega NN}^2 \, g_{\omega\sigma\omega}^2}{96\pi \, m_\omega^2} \, \frac{2t + 4m_N^2}{\lambda(s, m_\omega^2, m_N^2)} \, \frac{F_{\omega\sigma\omega}^2 \, F_{\omega NN}^2}{(t - m_\omega^2)^2} \left[(t - m_\omega^2 - m_\sigma^2)^2 - 4 m_\omega^2 m_\sigma^2 \right]. \tag{22}$$

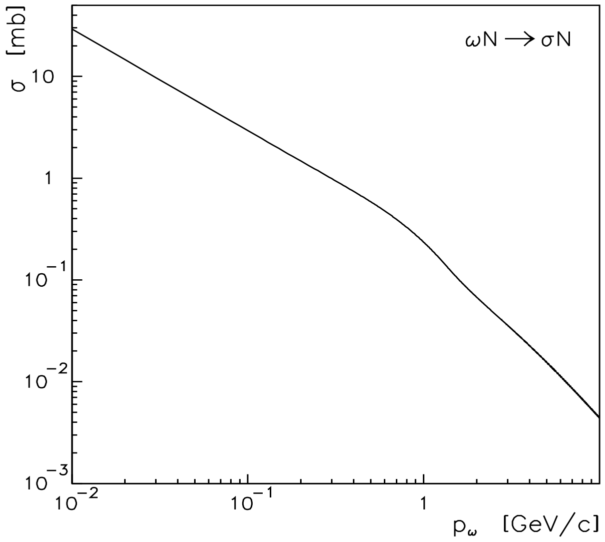

Fig. 11. The $\omega N \to \sigma N$ cross section within the ω-exchange model for $g_{\omega\sigma\omega}$=1.76.

We introduce a monopole form factor at the ωNN vertex with the cut-off Λ=1.5 GeV [39]. The parameters for the $\omega\sigma\omega$ vertex are the same as for the $\omega N \to \omega N$ calculations. This results in the $\omega N \to \sigma N$ cross section shown in Fig. 11, which also gives up to 30 mb for low ω momenta.

2.7 The total ωN cross section

We finally incoherently sum the partial cross sections - calculated for the different ωN reaction channels - and show the result in terms of the solid line in Fig. 12. In order to demonstrate the uncertainty due to the unknown coupling $g_{\omega\sigma\omega}$ we also show the total cross for $g_{\omega\sigma\omega}$=0 (dash-dotted line), i. e. neglecting the diagrams 1e) and 1f). In this limit the cross section is on average reduced by about 25%.

In this summation we have taken the cross section for the inclusive $\omega N \to \rho N X$ reaction instead of the exclusive $\omega N \to \rho \pi N$ reaction. Again at high momenta our result can be compared with the estimate from the Quark Model [47,48] obtained with Eq. (20) by replacing the elastic πN cross section with the total cross section. This result is shown by the dashed line in Fig. 12 and matches with our calculations in the OBE model at momenta of 0.5 GeV/c.

Furthermore, at high momenta the ωN total cross section can be estimated within the Vector Dominance Model, where the total ωN cross section can be related to the forward $\gamma N \to \omega N$ differential cross section as [50]

$$\sigma^2_{\omega N}(s) = \frac{\gamma^2_\omega}{4\pi}\frac{64\pi}{\alpha}\,\frac{1}{1+\alpha^2_\omega}\left(\frac{q_\gamma}{q_\omega}\right)^2 \left.\frac{d\sigma_{\gamma p\to\omega p}(s)}{dt}\right|_{t=0}, \quad (23)$$

where q_γ and q_ω are the photon and ω-meson momenta in the γN and ωN center-of-mass systems at the same invariant collision energy $\sqrt{s}$. In Eq. (23) α_ω denotes the ratio of the real to imaginary part of the ωN forward scattering amplitude [50], while g_ω is the $\gamma\omega$ coupling constant. We neglect α_ω and take $g^2_\omega/4\pi$=4.9 from Ref. [51]. The full circles (with error bars) in Fig. 12 show the total ωN cross section obtained from the experimental data on forward ω-meson photoproduction [51,52].

For the following transport calculations the total inelastic ωN cross section is separately fitted and interpolated as

$$\sigma_{inel} = 20 + \frac{4.0}{p_\omega}\ [\mathrm{mb}], \quad (24)$$

where the laboratory ω-meson momentum p_ω is given in GeV/c. The parameterization for the total ωN cross section then is given as a sum of the elastic (21) and inelastic (24) cross section as shown by the dotted line in Fig. 12. Especially the inelastic ωN cross section is found to be quite large at low momenta and implies substantial final state interactions of the ω-meson in the medium. This also holds for the limit $g_{\omega\sigma\omega}$=0.

In line with these final state interactions the ω-meson will change its spectral function in the medium and (in first order) will acquire a larger width due to collisional broadening at baryon density ρ_B,

$$\Gamma_{coll}(p_\omega) = \frac{4}{(2\pi)^3}\int d^3p\; v_{\omega N}\; \sigma_{\omega N}(\sqrt{s})\; \Theta(p_F - |\mathbf{p}|), \quad (25)$$

with $v_{\omega N}$ denoting the relative velocity between the ω-meson and the nucleon; p_F is the nuclear Fermi momentum and $\sqrt{s}$ the invariant energy of the ωN system.

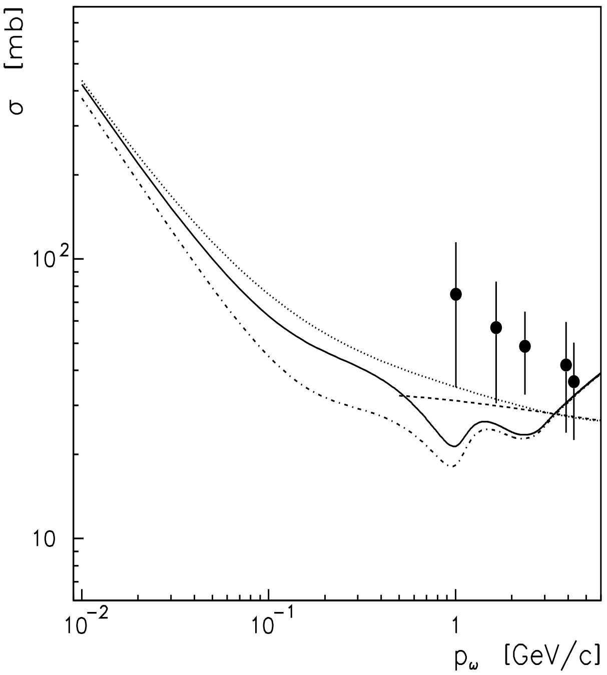

Fig. 12. The total ωN cross section as a function of the ω-meson momentum in the laboratory system. The solid line shows our result as an incoherent sum of the calculated partial cross sections; the dash-dotted line is obtained when omitting the diagrams 1e) and 1f), i.e. for $g_{\omega\sigma\omega}$=0. The full circles show the results obtained within the VDM from the data on forward ω-photoproduction. The dashed line illustrates the estimation from the Quark Model while the dotted line is our actual parameterization.

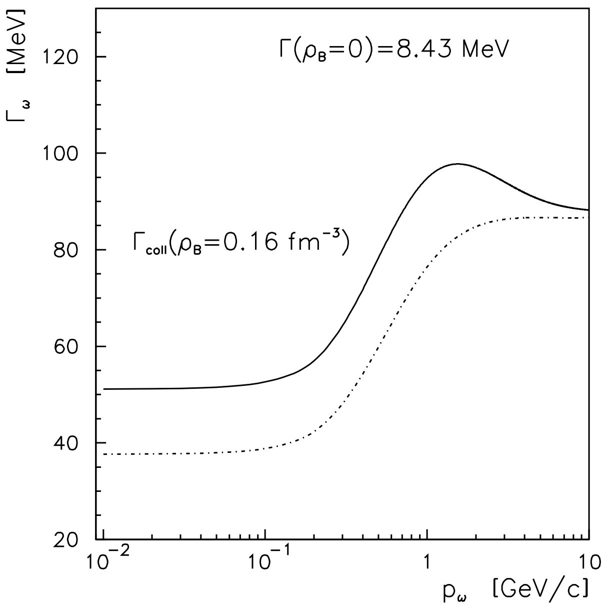

Fig. 13. The in-medium ω-meson width due to collisional broadening as a function of the laboratory ω-meson momentum. The solid line is obtained when including all channels while the dash-dotted line results for $g_{\omega\sigma\omega}$=0, i.e. neglecting diagrams 1e) and 1f).

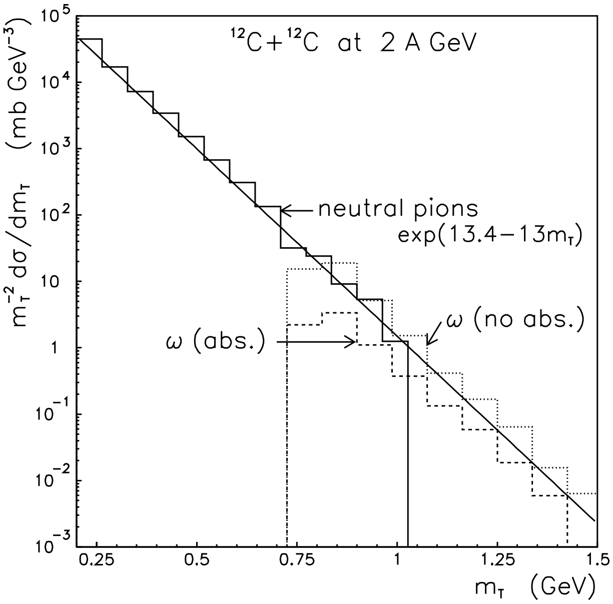

Fig. 14. The inclusive transverse mass spectra for π^0 (solid histogram) and ω-mesons (divided by a factor of 3 due to the ω polarizations) from $C{+}C$ collisions at 2 A·GeV. The dashed histogram shows the calculations with all ωN interactions while the dotted histogram is obtained without ω absorption. The thick solid line indicates the m_T-scaling.

The result for Γ_{coll} at density ρ_0 ($p_F{\approx}0.26$ GeV/c) is shown in Fig. 13 by the solid line as a function of the ω-meson momentum relative to the nuclear medium and is about 50 MeV at low ω momenta, but increases to 100 MeV above $p_\omega{\approx}1$ GeV/c. In the limit $g_{\omega\sigma\omega}$ = 0 (dash-dotted line) the collisional width is about 25% smaller up to relative momenta of 1 GeV/c; this represents the lower limit in our present approach. Our result is substantially larger at $p_\omega \approx 0$ than the estimate of 20 MeV in Ref. [16] and slightly larger than the result of Klingl et al. [14] due to the additional channels taken into account in our computations. Nevertheless, the collisional width for ω-mesons produced at rest in nuclei is still small compared to its mass.

3 ω-production in heavy-ion collisions

The production of ω-mesons from heavy-ion collisions has been calculated previously within the HSD transport approach [53] and is described e.g. in more detail in Ref. [4].

In these transport simulations the ω-absorption as well as elastic scattering in the nuclear environment are explicitely included as well as (optional) a reduction of the ω pole mass at finite baryon density. In the present study we concentrate on the impact of the ωN final state interactions with nucleons especially with respect to a global m_T-scaling suggested by Bratkovskaya et al. [53] for meson production from heavy-ion collisions at SIS energies. The latter scaling was found to be well in line with the spectra for π^0 and η mesons as measured by the TAPS Collaboration [54,55].

Employing the elastic and inelastic ωN cross sections from Section 2 we have performed calculations without ω-potentials in the medium for the systems ${}^{12}C{+}{}^{12}C$, ${}^{40}Ca{+}{}^{40}Ca$ at 2 A GeV and ${}^{58}Ni{+}{}^{58}Ni$ at 1.9 A·GeV, which are studied experimentally by the TAPS Collaboration also for ω-meson production via the Dalitz decay $\omega{\to}\pi^0\gamma$.

Figs. 14,15,16 show the calculated inclusive transverse mass spectra for π^0 and ω-mesons with the transverse mass defined as $m_T = \sqrt{p_T^2 + m^2}$, where p_T is the transverse momentum and m stands for the mass of the meson. The solid histograms in Figs. 14,15,16 show the π^0-meson spectra while the straight solid lines indicate the scaling

$$\frac{1}{m_T^2}\,\frac{d\sigma}{dm_T} = A\,\exp(-Bm_T) \tag{26}$$

with parameters A and B given in Table 1.

Indeed the neutral pions follow the scaling within the statistical accuracy. The transverse mass distributions for the ω-meson, which were divided by a factor of 3 as in Ref. [53] due to the 3 different polarizations of the ω-meson, are shown by the dotted histograms when neglecting the ω-meson absorption in nuclear matter due to the inelastic ωN interactions. In this limit the m_T-scaling is overestimated especially for $Ca{+}Ca$ and $Ni{+}Ni$. The dashed histograms show the calculations accounting for the ω-absorption as well as $\omega N{\to}\omega N$ elastic scattering. In all cases the m_T-scaling relative to neutral pions is underestimated especially for low transverse mass of the ω-mesons which results from the large absorption cross section for ω-mesons at low relative momenta according to Section 2.

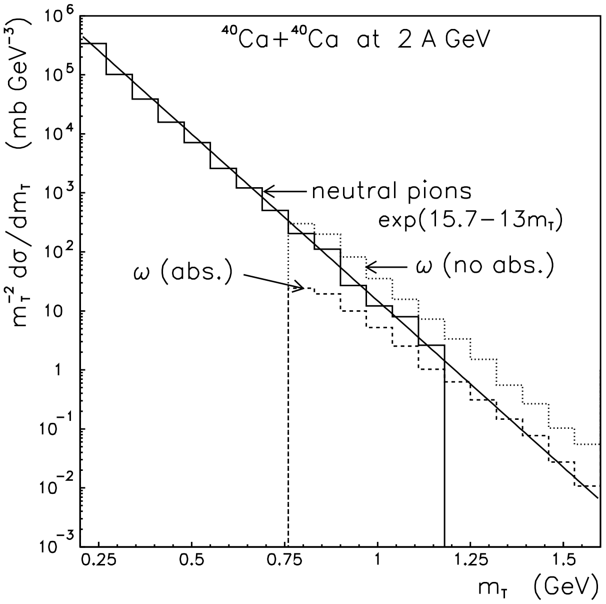

Fig. 15. The inclusive transverse mass spectra for π^0 (solid histogram) and ω-mesons (divided by the number of polarizations) from $Ca{+}Ca$ collisions at 2 A·GeV. The dashed histogram shows the calculations with all ωN interactions while the dotted histogram is obtained without ω absorption. The thick solid line indicates the m_T-scaling.

Table 1. Parameters of the m_T-scaling approximation (26).

System	$C+C$	$Ca+Ca$	$Ni+Ni$
Energy (A·GeV)	2.0	2.0	1.9
A (b·GeV^{-3})	660	6583	9821
B (GeV^{-1})	13	13	13

Table 2. Inclusive ω-meson production cross section from $C+C$, $Ca+Ca$ and $Ni+Ni$ collisions calculated with and without final state interactions of the ω mesons.

System	$C+C$	$Ca+Ca$	$Ni+Ni$
Energy (A·GeV)	2.0	2.0	1.9
σ (mb) with FSI	1.42	10.56	19.5
σ (mb) without FSI	6.52	91.4	206.8

Fig. 17 shows the nuclear transparency coefficient as a function of the ω-meson momentum in the center-of-mass for $C+C$, $Ca+Ca$ and $Ni+Ni$ systems. Here the nuclear transparency coefficient is defined as the ratio of the ω-mesons detected assymptotically for $t{\to}\infty$ to the total number of the ω-mesons produced in elementary pion-baryon and baryon-baryon collisions. The effect is most pronounced for slow ω-mesons since the inelastic ωN interaction is very strong at low momenta (cf. Fig. 12).

Table 2 shows the inclusive ω-meson production cross section for $C+C$, $Ca+Ca$ and $Ni+Ni$ collisions calculated with and without ωN final state interactions. Even for the light system $C+C$ the ω production cross section is reduced by a factor $\simeq$ 4.5 due to strong absorption.

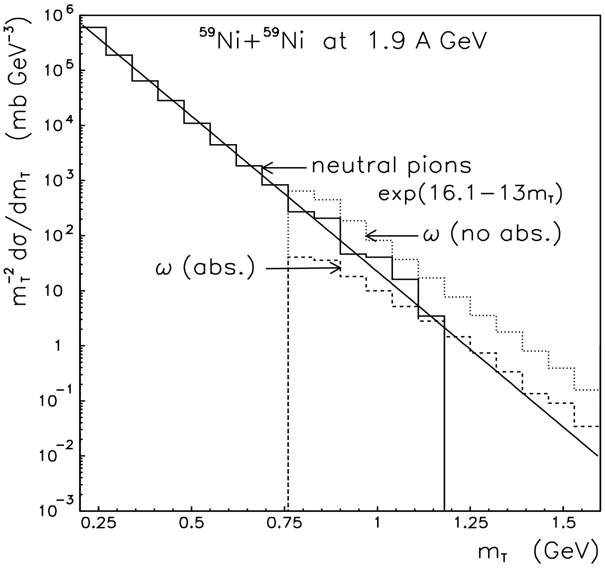

Fig. 16. The inclusive transverse mass spectra for π^0 (solid histogram) and ω-mesons from $Ni{+}Ni$ collisions at 1.9 A·GeV. The dashed histogram shows the calculations with all ωN interactions while the dotted histogram is obtained without ω absorption. The thick solid line indicates the m_T-scaling.

4 Summary

Within the meson exchange model we have calculated different partial cross sections for the ωN interaction, i.e. $\omega N{\to}\pi N$, $\omega N{\to}\rho N$, $\omega N{\to}\omega N$, $\omega N{\to}\rho\pi N$, $\omega N{\to}\rho NX$, $\omega N{\to}2\pi N$, $\omega N{\to}2\pi NX$ and $\omega N{\to}\sigma N$ reaction channels. The free parameters of the model were fixed by the available experimental data on the $\pi N{\to}\omega N$ reaction [24,30,31] or adopted from the study on vector meson photoproduction [20] except for the $\omega\sigma\omega$-vertex, where we have adopted a conservative low coupling constant; lower limits for our cross sections are obtained for $g_{\omega\sigma\omega}$ = 0. We note that the OBE calculations performed here do not correspond to *ab initio* calculations but serve as a convenient method to extrapolate from available data to unknown, but related channels. We estimate the relative error in the various cross sections to be within a factor of 2.

At high energies, i.e. ω momenta above a few GeV/c, the total cross section approaches a conventional hadronic cross section of $\simeq$ 25 mb according to the prediction from the Quark Model as well as the estimate from the Vector Dominance model. The total cross section at low ω momenta according to the OBE model sums up to a few hundred mb which indicates a sizeable rescattering and reabsorption of the ω-meson in the nuclear medium. The collisional broadening of the ω-meson at nuclear matter density ρ_0 amounts to 40 - 50 MeV at rest, but increases with momentum up to 80 - 100 MeV. Thus the ω spectral function at ρ_0 is dominated by the hadronic couplings in the medium. This statement holds also in view of the uncertainties still involved in the OBE approach.

Furthermore, we have investigated the impact of the ωN final state interactions on ω-production in heavy-ion collisions around 2 A·GeV. It is found that due to strong absorption the total ω-meson production cross section from $C+C$ collisions at SIS energies is reduced by a factor of $\simeq$4.5 and by a factor of $\simeq$10 for $Ni+Ni$ collisions. Furthermore, we find a significant deviation from the m_T-scaling behaviour predicted in Ref. [53] - where lower ωN cross sections from Ref. [11] had been employed - for ω-meson production in heavy-ion collisions due to the strong final state interactions for slow ω-mesons. These m_T distributions might be controlled by the TAPS Collaboration in near future and provide further experimental constraints on the ωN interaction.

The authors like to thank V. Metag and H. Löhner for valuable discussions throughout this study. Furthermore, they like to thank M. Post and G. Penner for pointing out a mistake in Eq. (3) in an earlier version of this manuscript. This work was supported by BMBF, Forschungszentrum Jülich and the Russia Foundation for the fundamental Research.

References

1. J.W. Harris and B. Müller, Ann. Rev. Nucl. Part. Sci. **46**, 71 (1996).
2. C.M. Ko and G.Q. Li, J. Phys. G **22**, 1673 (1996).
3. G.E. Brown and M. Rho, Phys. Rev. Lett. **66**, 2720 (1991).
4. W. Cassing and E.L. Bratkovskaya, Phys. Rep. **308**, 65 (1999).
5. S. Leupold, W. Peters and U. Mosel, Nucl. Phys. **A628**, 311 (1998).
6. R. Rapp, G. Chanfray and J. Wambach, Phys. Rev. Lett. **76**, 368 (1996); Nucl. Phys. **A617**, 472 (1997).
7. W. Peters, M. Post, H. Lenske, S. Leupold and U. Mosel, Nucl. Phys. **A632**, 109 (1998).
8. B. Friman and H.J. Pirner, Nucl. Phys. **A617**, 496 (1997).
9. W. Schön, H. Bokemeyer, W. Koenig and V. Metag, Acta Phys. Pol. B **27**, 2959 (1996).
10. W. Cassing, Ye.S. Golubeva, A.S. Iljinov and L.A. Kondratyuk, Phys. Lett. B **396**, 26 (1997).
11. Ye. S. Golubeva, L.A. Kondratyuk and W. Cassing, Nucl. Phys. **A625**, 832 (1997).
12. F. Klingl, N. Kaiser and W. Weise, Nucl. Phys. **A624**, 527 (1997).
13. F. Klingl and W. Weise, hep-ph/9802211.
14. F. Klingl, T. Waas and W. Weise, hep-ph/9810312.
15. B. Friman, nucl-th/9801053.
16. B. Friman, Acta Phys. Pol. B **29**, 3195 (1998).
17. W. Ehehalt and W. Cassing, Nucl. Phys. **A602**, 449 (1996).
18. M. Gell-Mann, D. Sharp and W.G. Wagner, Phys. Rev. Lett. **8**, 261 (1962).
19. N.M. Kroll, T.D. Lee and B. Zumino, Phys. Rev. **157**, 1376 (1967).
20. B. Friman and M. Soyeur, Nucl. Phys. **A600**, 475 (1996).
21. F. Klingl, N. Kaiser and W. Weise, Z. Phys. A **356**, 193 (1996); F. Klingl, private communication.
22. A. Sibirtsev, W. Cassing, G.I. Lykasov and M.V. Rzjanin, Nucl. Phys. **A632**, 131 (1998).
23. J.D. Jackson and H. Pilkuhn, Il Nuovo Cim. **33**, 906 (1964).
24. R. J. Miller, S. Lichtman and R.B. Willmann, Phys. Rev. **178**, 2061 (1969).
25. T.C. Bacon et al., Phys. Rev. **157**, 1263 (1967).
26. H.O. Cohn, W.M. Bugg and G.T. Condo, Phys. Lett. **15**, 344 (1965).
27. J.S. Danburg et al., Phys. Rev. D **2**, 2564 (1970).
28. F. Klingl, Ph.D. thesis, University of München, 1998.
29. K. Gottfried and J.D. Jackson, Il Nuovo Cim. **34**, 735 (1964).
30. L.E. Holloway et al., Phys. Rev. D **8**, 2814 (1973).
31. Landolt-Börnstein, New Series, ed. H. Schopper, I/12 (1988).
32. J.J. De Swart, M.C.M. Rentmeester and R.G.E. Timmermans, πN Newsletter **13**, 96 (1997).
33. A. Sibirtsev, K. Tsushima and A.W. Thomas, Phys. Lett. B **421**, 59 (1998).
34. V.B. Berestetsky and I.Ya. Pomeranchuk, Nucl. Phys. **22**, 629 (1961).
35. E. Ferrari and F. Selleri, Suppl. Nuovo Cim. **24**, 451 (1962).
36. A. Engel et al., Nucl. Phys. **A603**, 387 (1996).
37. A. Sibirtsev, W. Cassing and U. Mosel, Z. Phys. **A358**, 357 (1997).
38. L. A. Kondratyuk, A. Sibirtsev, W. Cassing, Ye. S. Golubeva, and M. Effenberger, Phys. Rev. C **58**, 1078 (1998).
39. R. Machleid, K. Holinde and Ch. Elster, Phys. Rep. **149**, 1 (1987).
40. M. Post, private communication.
41. Particle Data Group, Eur. Phys. J. A **3**, 1 (1998).
42. K. Nakayama, A. Szczurek, C. Hanhart, J. Haidenbauer, and J. Speth, Phys. Rev. C **57**, 1580 (1998).
43. C. Hanhart, private communication.
44. Particle Data Group, Phys. Rev. D **54**, 1 (1996).
45. P. Singer, Phys. Rev. **128**, 2789 (1962); **130**, 2441 (1963); **161**, 1694 (1967).
46. S. Fajfer and R.J. Oakes, Phys. Rev. D **42**, 2392 (1990).
47. H.J. Lipkin, Phys. Rev. Lett. **16**, 1015 (1966).
48. K. Kajantie and J.S. Trefil, Phys. Lett. B **24**, 106 (1967).
49. Particle Data Group, Phys. Rev. D **50**, 1173 (1994).
50. T.H. Bauer, R.D. Spital, D.R. Yennie and F.M. Pipkin, Rev. Mod. Phys. **50**, 261(1978).
51. J. Ballam et al., Phys. Rev. D **7**, 3150 (1973).
52. Landolt-Börnstein, New Series, ed. H. Schopper, **8** (1973).
53. E.L. Bratkovskaya, W. Cassing and U. Mosel, Phys. Lett. B **424**, 244 (1998).
54. R. Averbeck et al., Z. Phys. A **359**, 65 (1997).
55. M. Appenheimer et al., GSI Annual Report 1996, 58.

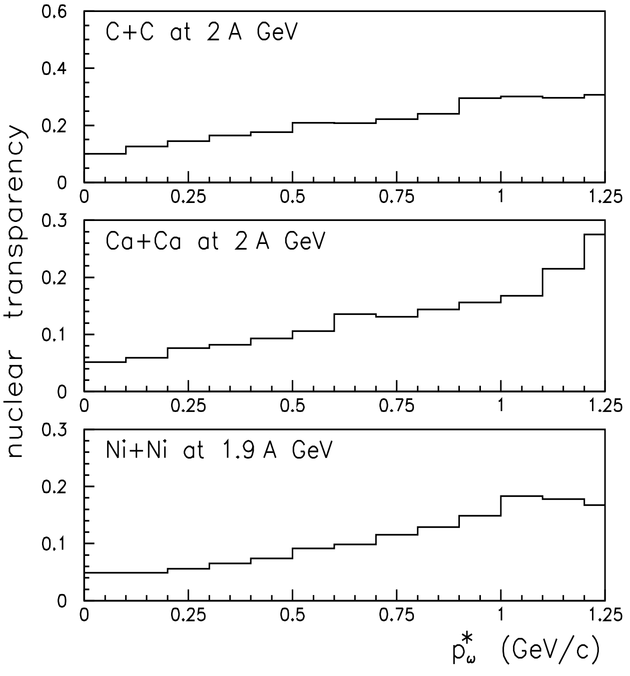

Fig. 17. The nuclear transparency coefficient as a function of the ω-momentum in the center-of-mass system for $C+C$, $Ca+Ca$ and $Ni+Ni$ collisions at 2.0 and 1.9 A GeV, respectively.